Interlayer-Exchange-Dominant Spin Hall Nano-Oscillator

Rongxin Li,[1] Xiaojuan Yuan,[1] Zhenhua Zhang,[2] Qian Chen,[3] Zhongming Zeng,[3] Zhihong Lu,[1,*] Ke Wang,[4] Yong Liu,[1,†] and Rui Xiong[1,‡]

[1] *Key Laboratory of Artificial Micro- and Nano-structures of Ministry of Education, School of Physics and Technology, Wuhan University, Wuhan 430072, People's Republic of China*

[2] *The State Key Laboratory of Refractories and Metallurgy, School of Materials and Metallurgy, Wuhan University of Science and Technology, Wuhan, 430081, People's Republic of China*

[3] *Key Laboratory of Multifunctional Nanomaterials and Smart Systems, Suzhou Institute of Nano-Tech and Nano-Bionics, CAS, Suzhou, Jiangsu 215123, People's Republic of China*

[4] *School of Mechanical and Electronic Engineering, East China University of Technology, Nanchang 330013, People's Republic of China*

(Received 20 July 2022; revised 24 October 2022; accepted 19 January 2023; published 7 March 2023)

The spin Hall nano-oscillator (SHNO) is a promising spintronic device to produce high-frequency and low-linewidth microwave signals. We study a type of SHNO based on the $L1_0$-FePt/NiFe/Pt exchange-spring system with an ultrahigh perpendicular magnetic anisotropy by micromagnetic simulation. The hard-soft magnetic exchange-spring system has a very high interlayer-exchange-interaction field, resulting in a more than 30-GHz emission frequency and 38.6-GHz/T field tunability. Apart from conventional localized and nonlocalized auto-oscillation modes, localized or nonlocalized modes with central antisymmetry also appear in this SHNO. Two oscillation centers possess nonequal amplitudes and opposite phases in these antisymmetrical modes. Different modes are determined by the competition between three factors: the exchange-interaction field, the perpendicular anisotropic field, and spin-orbit torque. The spin dynamics in the SHNO exhibit complex field and current dependence. Our results provide a possible direction for the design of SHNOs, which may be beneficial for the research and development of spintronic nano-oscillators.

DOI: 10.1103/PhysRevApplied.19.034020

I. INTRODUCTION

Sustained magnetization oscillation excited by a pure spin current has attracted much attention for years [1]. The spin Hall nano-oscillator (SHNO) [2] is a kind of spintronic device that exploits the localized pure spin current to drive persistent magnetization oscillation, which is similar to the spin-torque oscillator [3–5], except the spin polarization is replaced with a pure spin current produced by the spin Hall effect [6] or interface scattering (Rashba effect) [7]. In SHNOs, magnetization oscillation can be electrically detected through anisotropy magnetoresistance (AMR) [2] at the cost of output power. The exceptional frequency characteristics and auto-oscillation mode, like self-localized bullet and spin-wave modes, have been studied [8,9]. In previous studies on SHNOs, ferromagnet (FM)/heavy-metal structures like NiFe/Pt [1,2,10–12], NiFe/W [13], Co-Fe-B/W [8,14], Co-Fe-B/Pt [15], $[CoNi]_n$/Pt [16], and so on, were investigated. Moreover, a device composed of a single ferromagnetic layer, such as Al_2O_3(substrate)/NiFe [17], is also demonstrated to be a SHNO. Among these SHNOs, a high out-of-plane magnetic field is needed to reduce self-localization and form a nonlocalized spin-wave mode [8,9,18,19]. The application of a film with perpendicular magnetic anisotropy (PMA) may help to reduce the out-of-plane external field [20].

Here, we exploit the exchange interaction between NiFe ($Ni_{50}Fe_{50}$) and strongly perpendicular magnetic anisotropic $L1_0$-FePt [21–27] to take the place of the high out-of-plane field and excite the nonlocalized spin-wave modes in nanoconstricted SHNOs. $L1_0$-FePt is one of the ferromagnetic transition-metal alloys with the highest PMA and an easy axis along the [001] direction of the tetragonal lattice. The $L1_0$-FePt(hard magnet)/NiFe(soft magnet) bilayer film investigated here is a classic exchange-spring (ES) [28] system. The exchange interaction forces the magnetization of NiFe toward the out-of-plane direction and makes the spin precession in $L1_0$-FePt much easier. The dynamic behavior

*zludavid@live.com
†liuyong@whu.edu.cn
‡xiongrui@whu.edu.cn

 © 2023 American Physical Society

of the magnetization in NiFe is changed by the exchange interaction [29]. The frequency and spin-wave propagation of the $L1_0$-FePt/NiFe/Pt SHNO (ES SHNO) are only calculated under an in-plane magnetic field. In a $L1_0$-FePt/NiFe/Pt SHNO (ES SHNO), microwaves with a frequency beyond 30 GHz and tunability over 38.6 GHz/T can be obtained with the aid of a relatively low in-plane external field. Additionally, four auto-oscillation modes may be present in this system when varying the current and in-plane field. In addition to conventional localized spin-wave bullet and nonlocalized spin-wave modes, antisymmetric nonlocalized or localized modes are also found in this ES SHNO.

II. SIMULATION METHODS

The micromagnetic simulation is carried using the object-oriented micromagnetic framework (OOMMF) software. The Landau-Lifshitz-Gilbert equation with a spin-orbit-torque (SOT) term is

$$\frac{dm}{dt} = -\gamma(m \times H_{\text{eff}}) + \alpha\left(m \times \frac{dm}{dt}\right) + T_{\text{SOT}},$$

where

$$H_{\text{eff}} = H_{\text{ex}} + H_u + H + H_{\text{Oe}} - H_{\text{de}},$$

and

$$T_{\text{SOT}} = \gamma \frac{\hbar}{\mu_0 e} \frac{\theta_{\text{eff}} J}{2 t_f M_s}(m \times p \times m).$$

Here, γ is the gyromagnetic ratio, $\hbar$ is the reduced Planck constant, μ_0 is the vacuum permeability, e is the charge of an electron, M_s is the saturation magnetization, and $m = M/M_s$ is the reduced magnetization. H_{eff} is the effective field, including the exchange-interaction field, H_{ex}; H_u is the uniaxial anisotropic field; H_{de} is the demagnetization field; H is the external field; and H_{Oe} is the Oersted field. α is the Gilbert damping constant. T_{SOT} is the SOT generated from Pt and determined by the dampinglike torque efficiency, $\theta_{\text{eff}} = 0.08$, for the NiFe/Pt interface. $L1_0$-FePt cannot produce a spin current without a concentration gradient of Pt, and therefore, makes no contribution to the SOT [25,26]. J is the magnitude of the current density, and t_f is the thickness of the magnetic layer. **p** is the unit vector of the spin-polarization direction of the spin current. We consider only the dampinglike torque (DL torque) because the fieldlike torque originating from the NiFe/Pt interface is negligibly small [30]. In simulations, the saturation magnetizations of NiFe and $L1_0$-FePt are 860×10^3 and 690×10^3 A/m, respectively; the exchange-stiffness constants of NiFe and $L1_0$-FePt are 1.3×10^{-11} and 1.0×10^{-11} J/m, respectively; and the damping constants, α, of NiFe and $L1_0$-FePt are 0.02 and 0.01, respectively. The perpendicular anisotropic energy density of $L1_0$-FePt is 4×10^6 J/m^3 with an easy axis along the [001] direction, which is the surface normal of the film [22,27,29,31]. The anisotropic energy density of NiFe is set as zero. The current-density distribution and Oersted field in ES SHNO are calculated using COMSOL Multiphysics and then input into OOMMF to perform a more realistic simulation.

The configuration of the simulated SHNO is illustrated in Fig. 1(a), which has a total length × width of 1000×500 nm^2. The width of the nanoconstriction is 100 nm. The thicknesses of $L1_0$-FePt and NiFe are 2 and 4 nm, respectively, which are smaller than the exchange length of $L1_0$-FePt (about 5 nm). Current, I, flows along the $+x$ direction, and θ is the angle between the $+y$ axis and in-plane external field, H. To obtain an electrical output, we assume the AMR is 1 Ω, so that the total resistance is regulated by the angle between I and total magnetization ($\langle I, m\rangle$), as given by $R_{\text{total}} = R + \Delta R\cos^2(\langle I, m\rangle)$, as shown in Fig. 1(b), here ΔR means AMR. The electrical outputs are thus calculated by $V = IR + I\Delta R\cos^2(\langle I, m\rangle)$. Hence, the radio-frequency part is $V_{\text{rf}} = I\Delta R\cos^2(\langle I, m\rangle) = I\Delta R(M_x/M_s)^2$. The electrical frequency and amplitude of microwave emission can be obtained through processing the time-domain data of M_x/M_s by Fourier transform.

III. RESULTS AND DISCUSSION

According to the easy and hard M-H loops of the ES film shown in Fig. 1(c), the switching field, H_s, is 1.58 T and the nucleation field, H_n, is about 0.52 T. The switching field of the ES film is quite small due to the exchange-spring effect compared with that of a single-layer $L1_0$-FePt film (more than 9 T) [31]. The effective PMA of the ES film evaluated from the M-H loops is about 9.2×10^5 J/m^3, which is much lower than that of $L1_0$-FePt. Figure 1(d) shows the magnetization of each layer under an in-plane field, H, with $\theta = 45°$. When H increases, the x and y components of the magnetization of NiFe (M_{NiFe}) will increase significantly, which means M_{NiFe} has an obvious deviation towards to H. Meanwhile, the decrease of the z component suggests that the magnetization of the FePt layer (M_{FePt}) is also dragged towards H by H_{ex}. Additionally, the direction of M_{FePt} will also be affected by a perpendicular anisotropy field, H_u. H_{ex} is not constant and depends on the angle between magnetizations. It can be seen that the angle difference between M_{FePt} and M_{NiFe} is increased with increasing H, suggesting an enhancement of the interlayer-exchange field with the enlargement of H. Both H_u and H_{ex} will significantly affect the magnetization dynamics in ES SHNO when a driving current is injected.

After relaxation of the system, the magnetization dynamic behavior in ES SHNO is simulated under $H = 600$ mT, $\theta = 45°$, and three different currents of 5.5, 8.5, and 10.5 mA. The time and frequency domains of the oscillation spectra are shown in Fig. 2. It is obvious

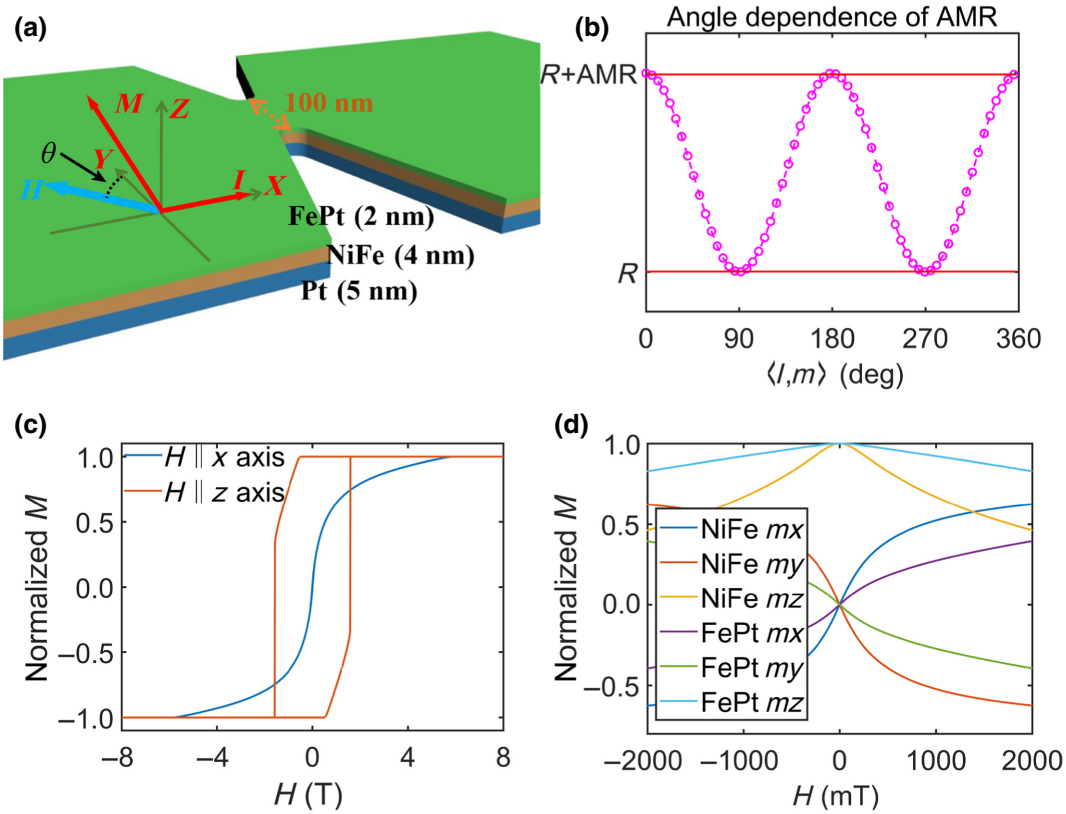

FIG. 1. (a) Schematic diagram of $L1_0$-FePt/NiFe/Pt SHNO under an in-plane field. (b) Diagram of angle dependence of AMR. (c) Total M-H loops of SHNO shown in (a). (d) Field dependence of magnetization components of the two ferromagnetic layers under an in-plane field with $\theta = 45°$.

that the oscillations of M_{FePt} and M_{NiFe} are completely synchronous due to the large enough interlayer-exchange interaction, but the amplitude of the oscillation of M_{FePt} is lower than that of M_{NiFe}. When the current increases from 5.5 to 8.5 mA, the oscillation amplitude of each ferromagnetic layer increases, corresponding to an increased electrical output, as seen in Figs. 2(a) and 2(b), right. The main frequencies are 34.87 GHz with 0.067-mV amplitude for 5.5 mA, and 35.26 GHz with 0.080-mV amplitude for 8.5 mA. The linewidths of the SHNO are all located in the range of 75–85 MHz. The obtained low linewidths agree with the general properties of SHNOs. The high-frequency oscillation obtained in ES SHNO is in good contrast to that of NiFe/Pt systems, which only produce 5–10-GHz oscillation frequency under the same field. According to the Kittle formula [32], a higher effective field will result in a higher magnetization-precession frequency. The much higher frequency is thus attributed to the much larger H_{eff} in the ES system than in NiFe/Pt systems. The enhancement of H_{eff} originates from the strong interlayer-exchange interaction and the extremely high anisotropy field of FePt. It is noteworthy that the electrical amplitude of the main frequency, as the current is increased to 10.5 mA, sharply decreases to a low value; meanwhile, the second-harmonic signal becomes remarkable, as shown in Fig. 2(c). Due to the relatively strong second-harmonic signal, the waveform is also not a typical sinelike wave. The main frequency in this case is 37.56 GHz with 0.021-mV amplitude, and the second harmonic is 75.02 GHz with 0.009 mV. In contrast to a relatively small increase (about 0.4 GHz) as the current increases from 5.5 to 8.5 mA, a large frequency increase (about 2.3 GHz) is observed when the current is enhanced from 8.5 to 10.5 mA. This kind of strong current-dependent oscillation behavior is related to the appearance of a special oscillation mode and is discussed later.

The field dependence and current dependence of the output spectra of an ES SHNO are investigated and shown in Fig. 3. Figure 3(a) is the field dependence of the main frequency of auto-oscillation at $I = 7$ mA and $\theta = 45°$. Under an applied field in the range of 500–700 mT, the oscillation has a typical sinelike waveform, with the main frequency increasing with external field. This kind of field dependence of frequency is widely reported in NiFe/Pt, Co-Fe-B/Pt [15], and Co-Fe-B/W [8]. The field tunability is approximately 38.6 GHz/T, which is much higher than the value of 12.14 GHz/T [17] obtained in the NiFe/Pt system. The high field tunability is attributed to H_{eff} in the

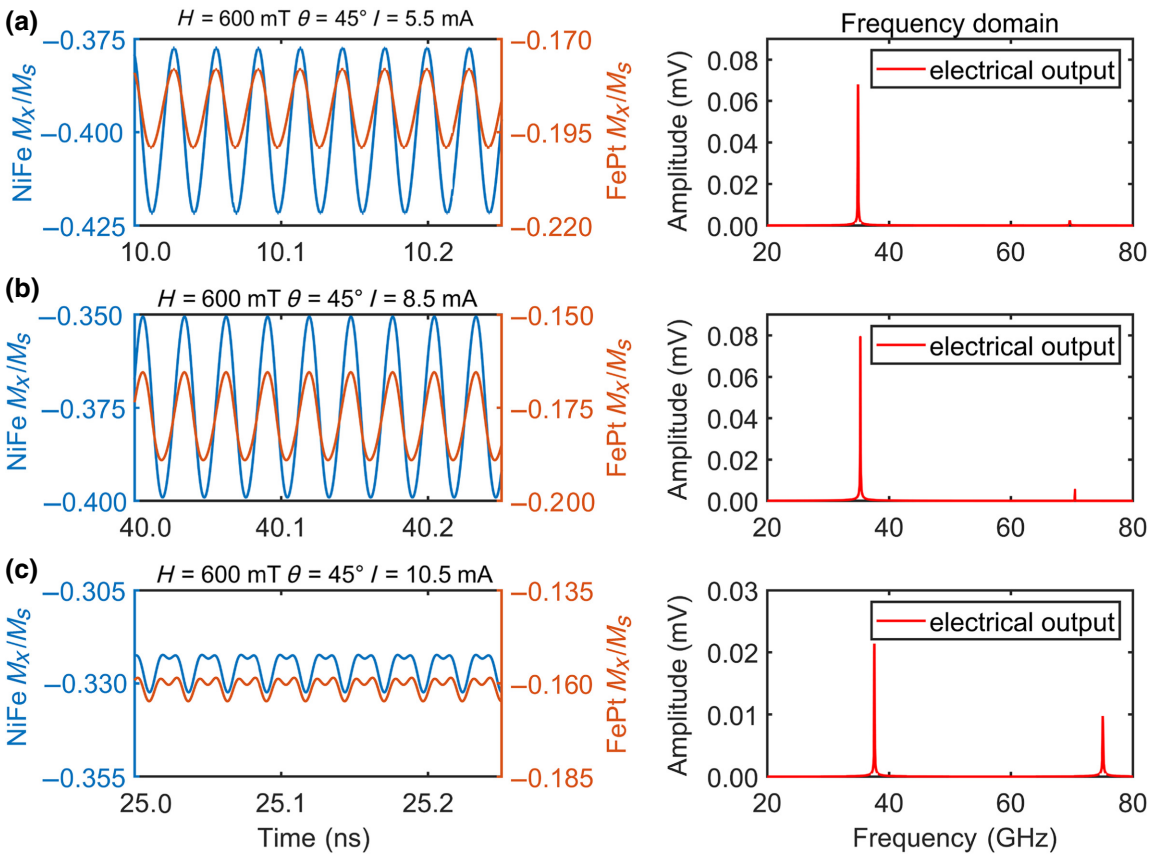

FIG. 2. (a)–(c) Time-domain (left) and frequency-domain (right) diagrams of an ES SHNO under a field of $H = 600$ mT and $\theta = 45°$ and currents of $I = 5.5$, 8.5, and 10.5 mA, respectively.

ES system varying much faster than the applied in-plane H, as discussed before. Figures 3(b)–3(d) show the current dependences of frequency and amplitude under three different fields with $\theta = 45°$. The working currents for these three conditions are all above 4 mA, higher than that of Pt/NiFe (1–2 mA), indicating that a much higher SOT is required to drive spin oscillation in the NiFe/FePt ES system. The large working current can be attributed to high H_{eff} in the ES system. The precession frequency dm/dt increases with H_{eff}, leading to an enhancement of the damping torque ($\alpha m \times dm/dt$). Therefore, a larger current is needed to offset the damping torque. A sudden jump in frequency and a fast drop in amplitude are observed in the spectra for $H = 550$ and 600 mT, while, in that for $H = 650$ mT, the frequency changes continuously without any sudden jump. These sudden changes are typical indications of the waveform transform shown in Figs. 2(b) and 2(c). The transition currents are 8.5 mA for 550 mT and 9.5 mA for 600 mT. It seems that this mode transformation occurs at a relatively low in-plane field and disappears as the field is larger than some value between 600 and 650 mT. Meanwhile, the current tunabilities of frequency in the low-amplitude regions shown in Figs. 3(b) and 3(c) are positive, indicating the oscillation modes are nonlocalized. The current tunabilities of frequency in the high-amplitudes regions shown in Figs. 3(b)–3(d) are nonmonotonic. The existence of a minimum frequency indicates the occurrence of the mode transition from a localized to a nonlocalized one. Figure 3(e) shows the spectrum under $H = 600$ mT and $\theta = 60°$. There is only a low-amplitude mode existing, and the frequency increases monotonously with the current, indicating that the mode is nonlocalized. For the case of $H = 800$ mT and $\theta = 85°$, as shown in Fig. 3(f), the relationship between spectra and current becomes rather complex—three regions are separated by two sudden jumps as the current increases. In the first region from 6 to 8 mA, the coexistence of the negative-current tunability and low amplitude, which is quite different from the spectra shown in Figs. 3(b)–3(e), indicates the appearance of a different type of localized mode. The second region from 8.5 to 16.5 mA and the third from 17 to 20 mA show phenomena similar to that in Figs. 3(b) and 3(c). As shown in Figs. 3(g)–3(i), the sudden jumps of frequency also occur when the direction of the in-plane component of M_{NiFe} is changed. In all regions, the frequencies decrease as θ increases. The θ dependences of the spectra indicate that the direction of the field also plays a role in spin-precession regulation. All

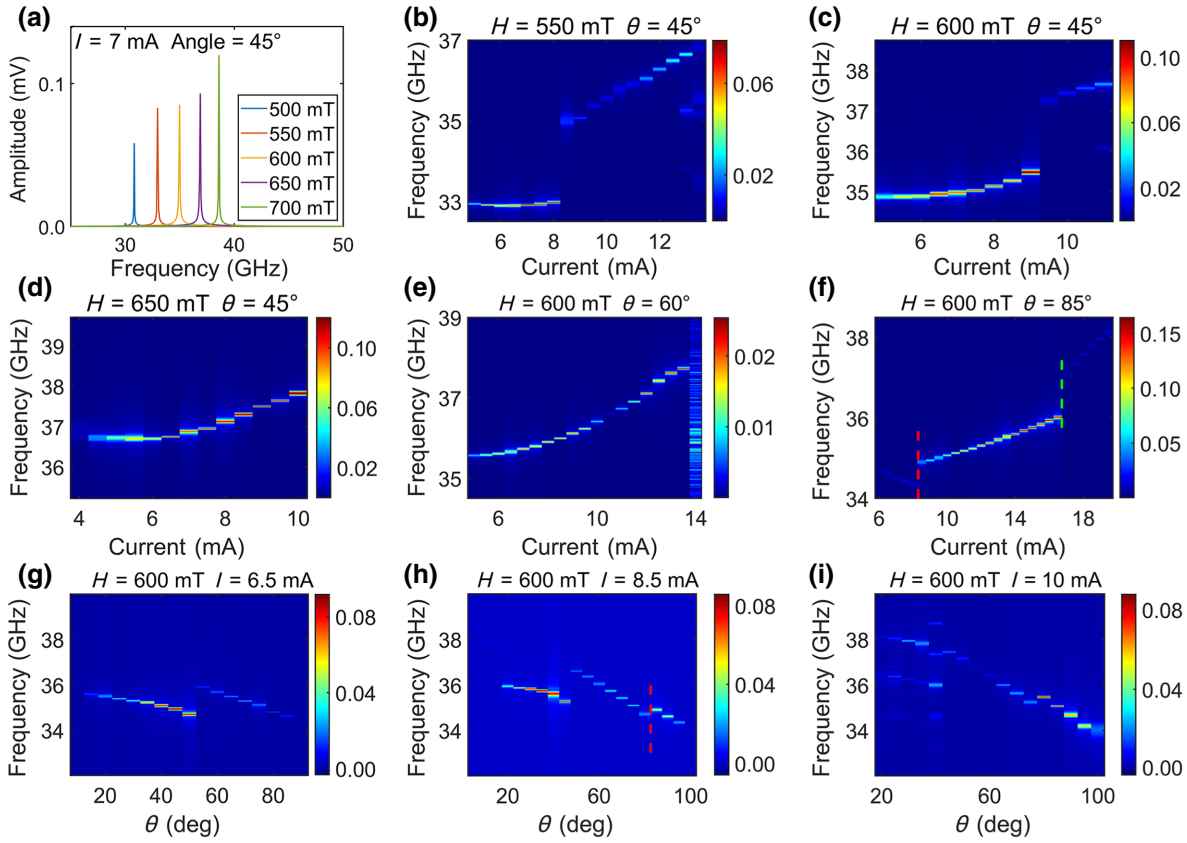

FIG. 3. Influences of the magnitudes of field (a), current (b)–(f), and angle of the field (g)–(i) on the output spectra of an ES SHNO.

spectra shown in Fig. 3 suggest that different oscillation modes may occur, depending on the field or SOT. At the transition point, frequency and amplitude will be subject to a sudden change.

Six types of magnetization configuration, corresponding to different oscillation modes, may occur with changes to the current and field, as displayed in Fig. 4. The six oscillation patterns are extracted from Fig. 3 and can be divided into four types of modes according to localization and symmetry. The four types of mode are localized symmetrical mode [Fig. 4(a)], nonlocalized-symmetrical mode [Figs. 4(b) and 4(e)], localized antisymmetrical mode [Fig. 4(d)], and nonlocalized antisymmetrical mode [Figs. 4(c) and 4(f)]. All the patterns shown in Fig. 4 include two relatively independent oscillations originating from the upper or bottom edges of the nanoconstriction. They can be taken as a pair of oscillation centers because local maxima of the current density are also present at the two edges. The intralayer-exchange field tends to fuse two centers to form bigger one. Hence, the formation of an oscillation-center pair may be attributed to the large out-of-plane interlayer-exchange field, which can force M_{FePt} and M_{NiFe} in the nanoconstriction to precess around their respective H_{eff}, which have a high-z component. Due to the high-z component of M_{NiFe}, the in-plane intralayer-exchange field between two oscillation centers is relatively small and can be overcome by the interlayer-exchange field. As a result, the relative independence of two oscillation centers can be maintained. The existence of a pair of oscillation centers should be the precondition for the occurrence of antisymmetrical modes, while competition between intralayer exchange and interlayer exchange determines the final mode of the ES SHNO—a high interlayer-exchange field prefers antisymmetrical modes, while a high intralayer-exchange field prefers symmetrical modes. The reason why the antisymmetrical mode appears under a low in-plane H can be thus attributed to the relatively small in-plane intralayer-exchange field due to the high-z component of M_{NiFe}. In the antisymmetrical mode [Figs. 4(c), 4(d), and 4(f)], the phases of two oscillation centers are opposite (red versus blue in pattern). Accordingly, the oscillations of magnetization originating from two oscillation centers are also opposite in phase and almost compensate for each other. This is the reason for the appearance of low-amplitude regions in the spectra, as shown in Fig. 3. For the nonlocalized symmetrical mode [Figs. 4(b) and 4(e)] and the nonlocalized antisymmetrical mode [Figs. 4(c) and 4(f)], it can be found that a change in the direction of in-plane H will dramatically change the wavelength. The short-wavelength modes shown in

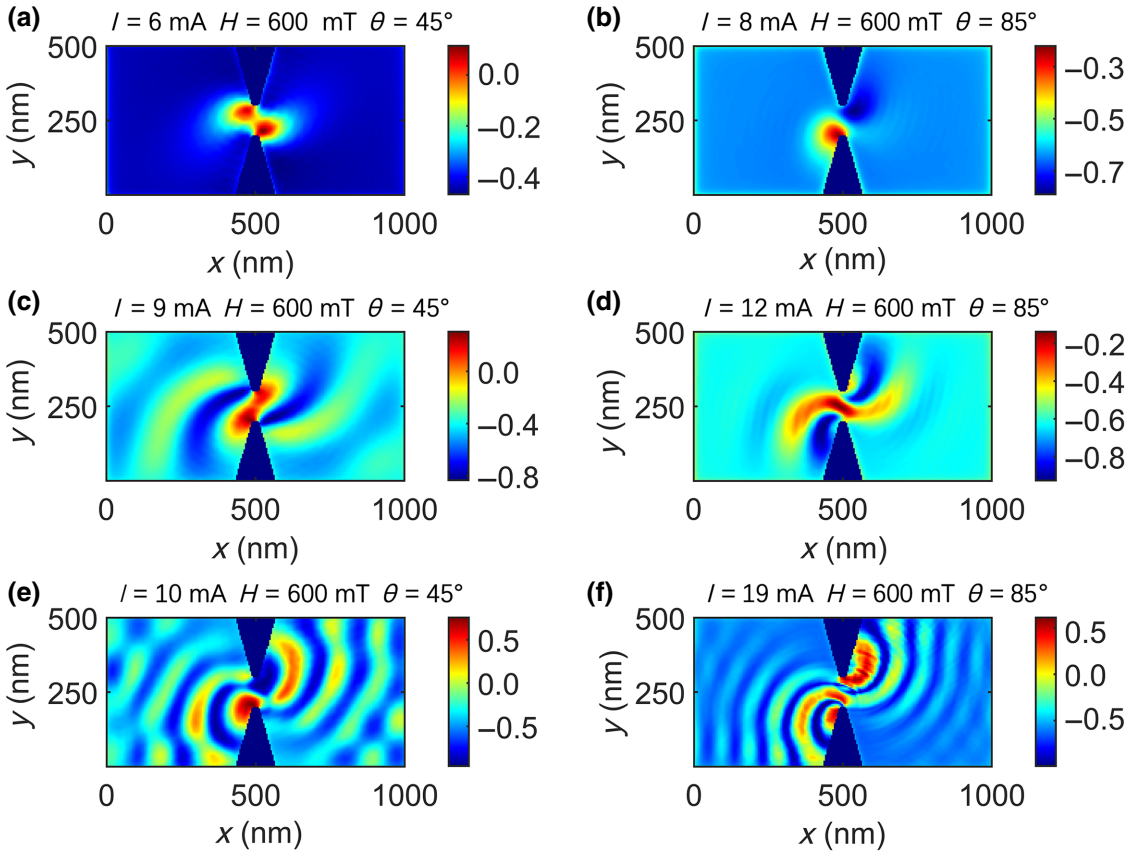

FIG. 4. Four oscillation modes in ES SHNO; all patterns are the oscillations of M_x/M_s. (a) Localized symmetrical mode; (b) localized antisymmetrical mode; (c) nonlocalized symmetrical mode; (e) nonlocalized antisymmetrical mode. (d),(f) Two special short-wavelength nonlocalized symmetrical mode and antisymmetrical mode respectively, they appear only when θ exceeds a certain value.

Figs. 4(e) and 4(f) appear only when H is close to the $-x$ direction. A short-wavelength nonlocalized symmetrical mode can be transformed from a localized antisymmetrical mode, as marked with red dashed lines in Figs. 3(f) and 3(h), and changed into a short-wavelength nonlocalized antisymmetrical mode with increasing current, as indicated by the green dashed line in Fig. 3(f). According to the geometrical relationship of SOT ($m \times p \times m$), the increase of the x component of magnetization caused by near-x-direction H will enhance the magnitude of SOT. A large SOT may also be beneficial for overcoming the intralayer exchange and maintaining the independence of the two oscillation centers, considering that the intralayer-exchange field of a short-wavelength mode is larger than that of a normal-wavelength mode.

To verify the causality between the antisymmetrical modes and the exchange field, the microwave outputs of the ES SHNO with nanoconstriction widths of 140 or 60 nm are calculated under $H = 600$ mT, $\theta = 45°$, and the results are shown in Fig. 5. Compared with that in an ES SHNO with a nanoconstriction width of 100 nm, the current density in the one with the 60-nm nanoconstriction width is higher. As shown in Figs. 3(b) and 3(c), it is expected that a higher current density would result in a lower transition current. However, the sudden jump of frequency or amplitude happens under a larger current for the ES SHNO with 60-nm nanoconstriction. The enhancement of the transition current with decreasing nanoconstriction width is likely to result from the increase of the intralayer-exchange field between two oscillation centers

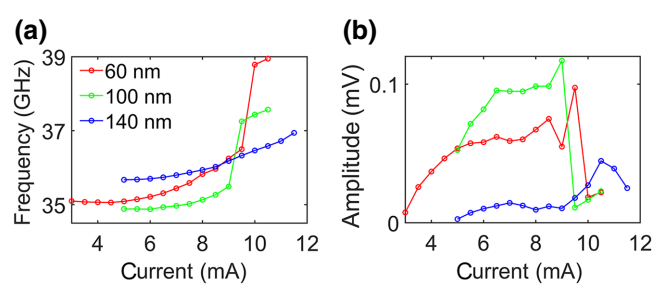

FIG. 5. Current dependences of frequency (a) and amplitude (b) of three ES SHNOs with different widths of nanoconstrictions under $H = 600$ mT, $\theta = 45°$.

due to the decrease in the separation of them. For the ES SHNO with the 140-nm nanoconstriction width, no sudden jump is observed in either frequency or amplitude, and the amplitudes are obviously lower than those of the symmetrical mode obtained in the ES SHNO with 60- or 100-nm constrictions. Actually, in the ES SHNO with the 140-nm nanoconstriction width, no symmetrical mode is produced, and the amplitudes of the oscillations are consistently low and comparable with those of the antisymmetrical mode observed for the 60- or 100-nm constriction widths, as shown in Fig. 5(b). The different oscillation behaviors of ES SHNOs with different nanoconstriction widths suggest that the antisymmetrical mode is likely to be determined by competition between the interlayer-exchange field and intralayer-exchange field around the oscillation centers. With an increase of the separation between two centers, the intralayer-exchange field between them diminishes, and the oscillation prefers the antisymmetrical mode. Therefore, the applied current plays a role in modulating the symmetry of the oscillation mode in an ES SHNO with a relatively narrow nanoconstriction.

If the two oscillation centers in the antisymmetrical mode are of perfect antiphase and have the same amplitude, the total amplitude of the SHNO is expected to be zero, rather than a finite value, as shown in Figs. 2–4. Figure 6(a) shows the magnetization oscillation in the upper half and bottom half of the nanoconstriction under $H = 600$ mT, $\theta = 85°$, and $I = 6.5$ mA. There is a phase difference close to 180° between the two areas, but the amplitudes of the two areas are not equal, which results in a nonzero total amplitude. The nonequal amplitudes of the two antiphase oscillations explain the finite amplitude of the antisymmetrical mode. Then the detailed process of the oscillation-mode change is considered. In the ES SHNO, the intralayer-exchange field, $H_{\mathrm{ex,in}}$; interlayer-exchange field, $H_{\mathrm{ex,inter}}$; and ultrahigh H_u of FePt will act on two oscillation centers and make H_{eff} much more complex than that in a conventional SHNO. Figure 6(b) shows the distributions of the magnetization z component of NiFe and H_u of FePt in an antisymmetrical nonlocalized mode. It can be seen that the variation of H_u during oscillation is more than 2.5 T at the oscillation centers. It is expected that $H_{\mathrm{ex,inter}}$ and $H_{\mathrm{ex,in}}$ are also subject to a large variation. Figure 6(c)

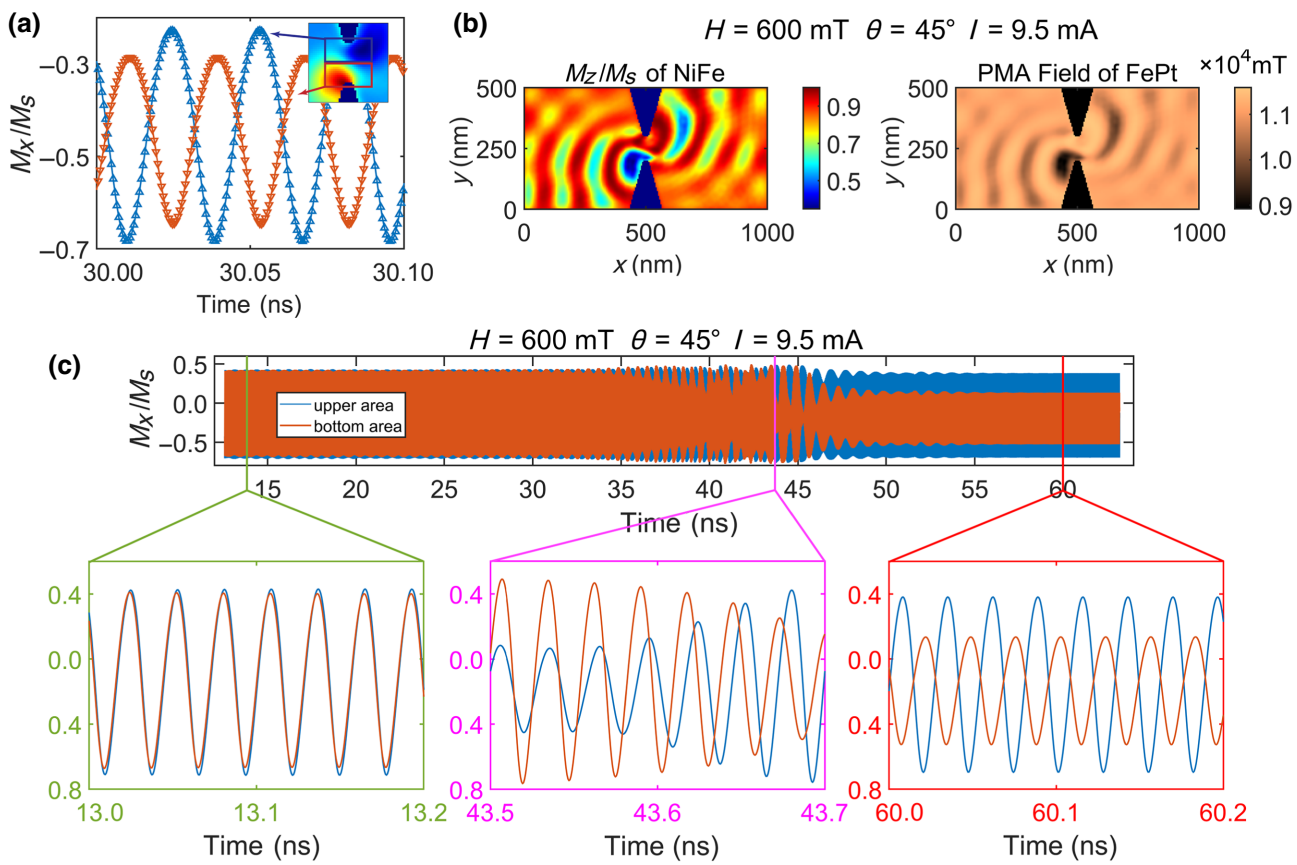

FIG. 6. (a) Magnetization-oscillation processes in the two half areas of nanoconstriction. Blue box is the upper area, and red box is the bottom area of nanoconstriction shown in the inset. (b) Left, distribution of the z component of M_{NiFe} at a certain time point with a configuration of $H = 600$ mT, $\theta = 45°$, and $I = 9.5$ mA; right, distribution of the PMA field (H_u) of FePt at the same time point as that shown to the left. (c) Total time–oscillation-process curve; upper and bottom areas match those shown in the inset of (a).

shows the detailed process from the symmetrical mode to the antisymmetrical mode. As shown, for three different time durations, the oscillation starts from a symmetrical mode. However, due to the small deviation induced by the enhanced SOT, this mode is not stable and the instability enhances with time. The oscillation finally stabilizes in an antisymmetrical mode with drastic changes in frequency and amplitude. In consideration of the initial unstable symmetrical mode, the reason for the mode change may be as follows: with an increase of the SOT, the variations of H_u, $H_{\mathrm{ex,inter}}$, and $H_{\mathrm{ex,in}}$ exceed the dynamic stable range of the symmetrical mode, so that the mode transits to an antisymmetrical one, which allows a larger variation of the three kinds of fields mentioned above during oscillation. After stabilization of the antisymmetrical mode, H_{eff} becomes higher, resulting in a sudden jump in frequency. In real devices, H_{eff} is also affected by temperature. Joule heating produced by a large working current may also be an issue that needs to be considered. The increase of temperature resulting from the Joule effect will lead to a decrease of the saturation magnetization and PMA energy, especially at the nanoconstriction. A reduction of the PMA energy will mean that M_{FePt} can be more easily dragged by an in-plane field. Therefore, Joule heating will lead to decreases of H_u, $H_{\mathrm{ex,inter}}$, and H_{eff}. It can be expected that the frequency of microwave emission will be lowered, and the conditions (driving current, amplitude and direction of magnetic field, etc.) for the occurrences of the modes may change. According to our previous discussion, the deceases of H_u and $H_{\mathrm{ex,inter}}$ may be unfavorable for antisymmetrical modes. It is hard to evaluate well through the micromagnetic simulation; however, practically, the effect of Joule heating can be diminished by improving the DL torque efficiency. In our simulation, the DL torque efficiency is only 0.08. For materials with strong SOC, such as a topological insulator or some special alloys [33–35], a much higher DL torque efficiency can be obtained. Temperature change also brings about an equivalent randomly fluctuating field, H_T, which is not considered in our simulations. Considering that the magnitude of H_T is usually about 1–5 mT at 300 K [36], this temperature-related fluctuating field is very likely to act as a small perturbation, which may increase the linewidth of microwave emission. According to our study, H_T may also affect the stability of a mode and prompt the transitions between different modes. As shown in Fig. 6(c), the oscillation begins with the unstable symmetrical mode; the introduction of H_T tends to exaggerate this instability and prompt the transition from a symmetrical mode to an antisymmetrical mode.

As presented above, complex spin dynamics may occur in an exchange-coupled NiFe/$L1_0$-FePt bilayer system due to the complex H_{eff}. SHNOs based on this kind of bilayer not only produce a high oscillation frequency but also create more oscillation modes than a normal Pt/FM SHNO.

IV. CONCLUSION

We study a nanoconstricted SHNO based on the $L1_0$-FePt/NiFe/Pt exchange-spring system using micromagnetic simulation. By the introduction of a high perpendicular magnetic anisotropic field and the interlayer-exchange interaction, the oscillation frequency is enhanced to more than 30 GHz under only 500-mT in-plane field and the average field tunability is 38.6 GHz/T. In this SHNO, not only can the conventional oscillation modes—the symmetrical localized mode and symmetrical nonlocalized mode—be observed, but also antisymmetrical modes, either localized or nonlocalized, may appear by varying the excitation conditions. By investigating the magnetization configuration in nanoconstriction during oscillation, we find, in antisymmetrical modes, antiphase oscillations of two oscillation centers have nonequal amplitude, leading to finite total oscillation of these modes. The antisymmetrical mode is found to be formed by the balance of three factors: the perpendicular magnetic anisotropic field, the exchange-interaction field, and SOT. Our results provide a possible direction for the design of SHNOs that may be beneficial for further studies on spintronic oscillators and applications.

ACKNOWLEDGMENTS

This work is supported by the National Natural Science Foundation of China (Grants No. 91963207 and No. 51871170)

[1] V. E. Demidov, S. Urazhdin, H. Ulrichs, V. Tiberkevich, A. Slavin, D. Baither, G. Schmitz, and S. O. Demokritov, Magnetic nano-oscillator driven by pure spin current, Nat. Mater. **11**, 1028 (2012).

[2] R. H. Liu, W. L. Lim, and S. Urazhdin, Spectral Characteristics of the Microwave Emission by the Spin Hall Nano-Oscillator, Phys. Rev. Lett. **110**, 147601 (2013).

[3] Z. Zeng, G. Finocchio, and H. Jiang, Spin transfer nano-oscillators, Nanoscale **5**, 2219 (2013).

[4] N. Locatelli, V. Cros, and J. Grollier, Spin-torque building blocks, Nat. Mater. **13**, 11 (2014).

[5] D. Houssameddine, U. Ebels, B. Delaet, B. Rodmacq, I. Firastrau, F. Ponthenier, M. Brunet, C. Thirion, J. P. Michel, L. Prejbeanu-Buda, *et al.*, Spin-torque oscillator using a perpendicular polarizer and a planar free layer, Nat. Mater. **6**, 441 (2007).

[6] J. Hirsch, Spin Hall Effect, Phys. Rev. Lett. **83**, 1834 (1999).

[7] A. D. Caviglia, M. Gabay, S. Gariglio, N. Reyren, C. Cancellieri, and J. M. Triscone, Tunable Rashba Spin-Orbit Interaction at Oxide Interfaces, Phys. Rev. Lett. **104**, 126803 (2010).

[8] H. Fulara, M. Zahedinejad, R. Khymyn, A. Awad, S. Muralidhar, M. Dvornik, and J. Åkerman, Spin-orbit

torque–driven propagating spin waves, Sci. Adv. **5**, eaax8467 (2019).

[9] S. Bonetti, V. Tiberkevich, G. Consolo, G. Finocchio, P. Muduli, F. Mancoff, A. Slavin, and J. Akerman, Experimental Evidence of Self-Localized and Propagating Spin Wave Modes in Obliquely Magnetized Current-Driven Nanocontacts, Phys. Rev. Lett. **105**, 217204 (2010).

[10] A. A. Awad, P. Dürrenfeld, A. Houshang, M. Dvornik, E. Iacocca, R. K. Dumas, and J. Åkerman, Long-range mutual synchronization of spin Hall nano-oscillators, Nat. Phys. **13**, 292 (2016).

[11] P. Durrenfeld, A. A. Awad, A. Houshang, R. K. Dumas, and J. Akerman, A 20 nm spin Hall nano-oscillator, Nanoscale **9**, 1285 (2017).

[12] M. Zahedinejad, A. A. Awad, S. Muralidhar, R. Khymyn, H. Fulara, H. Mazraati, M. Dvornik, and J. Akerman, Two-dimensional mutually synchronized spin Hall nano-oscillator arrays for neuromorphic computing, Nat. Nanotechnol. **15**, 47 (2020).

[13] H. Mazraati, S. Chung, A. Houshang, M. Dvornik, L. Piazza, F. Qejvanaj, S. Jiang, T. Q. Le, J. Weissenrieder, and J. Åkerman, Low operational current spin Hall nano-oscillators based on NiFe/W bilayers, Appl. Phys. Lett. **109**, 242402 (2016).

[14] M. Zahedinejad, H. Mazraati, H. Fulara, J. Yue, S. Jiang, A. A. Awad, and J. Åkerman, CMOS compatible W/CoFeB/MgO spin Hall nano-oscillators with wide frequency tunability, Appl. Phys. Lett. **112**, 132404 (2018).

[15] M. Ranjbar, P. Durrenfeld, M. Haidar, E. Iacocca, M. Balinskiy, T. Q. Le, M. Fazlali, A. Houshang, A. A. Awad, R. K. Dumas, *et al.*, CoFeB-based spin Hall nano-oscillators, IEEE Magn. Lett. **5**, 1 (2014).

[16] B. Divinskiy, V. E. Demidov, A. Kozhanov, A. B. Rinkevich, S. O. Demokritov, and S. Urazhdin, Nanoconstriction spin-Hall oscillator with perpendicular magnetic anisotropy, Appl. Phys. Lett. **111**, 082406 (2017).

[17] M. Haidar, A. A. Awad, M. Dvornik, R. Khymyn, A. Houshang, and J. Akerman, A single layer spin-orbit torque nano-oscillator, Nat. Commun. **10**, 2362 (2019).

[18] G. Consolo, L. Lopez-Diaz, L. Torres, and B. Azzerboni, Magnetization dynamics in nanocontact current controlled oscillators, Phys. Rev. B **75**, 214428 (2007).

[19] A. Slavin and V. Tiberkevich, Spin Wave Mode Excited by Spin-Polarized Current in a Magnetic Nanocontact Is a Standing Self-Localized Wave Bullet, Phys. Rev. Lett. **95**, 237201 (2005).

[20] G. Gerhart, E. Bankowski, G. A. Melkov, V. S. Tiberkevich, and A. N. Slavin, Angular dependence of the microwave-generation threshold in a nanoscale spin-torque oscillator, Phys. Rev. B **76**, 024437 (2007).

[21] C.b. Rong, D. Li, V. Nandwana, N. Poudyal, Y. Ding, Z. L. Wang, H. Zeng, and J. P. Liu, Size-dependent chemical and magnetic ordering in $L1_0$-FePt nanoparticles, Adv. Mater. **18**, 2984 (2006).

[22] F. Casoli, L. Nasi, F. Albertini, S. Fabbrici, C. Bocchi, F. Germini, P. Luches, A. Rota, and S. Valeri, Morphology evolution and magnetic properties improvement in FePt epitaxial films by *in situ* annealing after growth, J. Appl. Phys. **103**, 043912 (2008).

[23] O. Ivanov, Determination of the anisotropy constant and saturation magnetization, and magnetic properties of powders of an iron-platinum alloy, Phys. Met. Metallogr. **35**, 81 (1973).

[24] K. Son, G. Ryu, H. H. Jeong, L. Fink, M. Merz, P. Nagel, S. Schuppler, G. Richter, E. Goering, and G. Schutz, Superior magnetic performance in FePt $L1_0$ nanomaterials, Small **15**, e1902353 (2019).

[25] T. Seki, S. Iihama, T. Taniguchi, and K. Takanashi, Large spin anomalous Hall effect in $L1_0$−FePt: Symmetry and magnetization switching, Phys. Rev. B **100**, 144427 (2019).

[26] M. Tang, K. Shen, S. Xu, H. Yang, S. Hu, W. Lu, C. Li, M. Li, Z. Yuan, S. J. Pennycook, *et al.*, Bulk spin torque-driven perpendicular magnetization switching in $L1_0$FePt single layer, Adv. Mater. **32**, e2002607 (2020).

[27] S. Okamoto, N. Kikuchi, O. Kitakami, T. Miyazaki, Y. Shimada, and K. Fukamichi, Chemical-order-dependent magnetic anisotropy and exchange stiffness constant of FePt(001) epitaxial films, Phys. Rev. B **66**, 024413 (2002).

[28] G. Asti, M. Ghidini, R. Pellicelli, C. Pernechele, M. Solzi, F. Albertini, F. Casoli, S. Fabbrici, and L. Pareti, Magnetic phase diagram and demagnetization processes in perpendicular exchange-spring multilayers, Phys. Rev. B **73**, 094406 (2006).

[29] P. M. S. Monteiro and D. S. Schmool, Magnetization dynamics in exchange-coupled spring systems with perpendicular anisotropy, Phys. Rev. B **81**, 214439 (2010).

[30] M. Dvornik, A. A. Awad, and J. Åkerman, Origin of Magnetization Auto-Oscillations in Constriction-Based Spin Hall Nano-Oscillators, Phys. Rev. Appl. **9**, 014017 (2018).

[31] Y. Song, Z. Zhang, N. Duan, J. Wang, Y. Chen, B. Tong, X. Yang, and Y. Zhang, Composition and size dependence of magnetic properties of FePt/Fe exchange-spring films, J. Magn. Magn. Mater. **371**, 100 (2014).

[32] C. Herring and C. Kittel, On the theory of spin waves in ferromagnetic media, Phys. Rev. **81**, 869 (1951).

[33] H. Wu, P. Zhang, P. Deng, Q. Lan, Q. Pan, S. A. Razavi, X. Che, L. Huang, B. Dai, K. Wong, *et al.*, Room-Temperature Spin-Orbit Torque from Topological Surface States, Phys. Rev. Lett. **123**, 207205 (2019).

[34] N. H. D. Khang, Y. Ueda, and P. N. Hai, A conductive topological insulator with large spin Hall effect for ultralow power spin-orbit torque switching, Nat. Mater. **17**, 808 (2018).

[35] R. Li, X. Yuan, H. Tu, Z. Zhang, Y. Luo, Q. Chen, S. Li, S. Liang, Y. Liu, Z. Lu, *et al.*, High spin Hall conductivity induced by ferromagnet and interface, Adv. Funct. Mater. **32**, 2112754 (2022).

[36] K. Hayakawa, S. Kanai, T. Funatsu, J. Igarashi, B. Jinnai, W. A. Borders, H. Ohno, and S. Fukami, Nanosecond Random Telegraph Noise in In-Plane Magnetic Tunnel Junctions, Phys. Rev. Lett. **126**, 117202 (2021).